

Two-color Fermi-liquid theory for transport through a multilevel Kondo impurityD. B. Karki,^{1,2} Christophe Mora,³ Jan von Delft,⁴ and Mikhail N. Kiselev¹¹*The Abdus Salam International Centre for Theoretical Physics (ICTP), Strada Costiera 11, I-34151 Trieste, Italy*²*International School for Advanced Studies (SISSA), Via Bonomea 265, 34136 Trieste, Italy*³*Laboratoire Pierre Aigrain, École Normale Supérieure, PSL Research University, CNRS, Université Pierre et Marie Curie, Sorbonne Universités, Université Paris Diderot, Sorbonne Paris-Cité, 24 rue Lhomond, 75231 Paris Cedex 05, France*⁴*Physics Department, Arnold Sommerfeld Center for Theoretical Physics and Center for NanoScience, Ludwig-Maximilians-Universität München, 80333 München, Germany*

(Received 8 February 2018; revised manuscript received 18 April 2018; published 2 May 2018)

We consider a quantum dot with $\mathcal{K} \geq 2$ orbital levels occupied by two electrons connected to two electric terminals. The generic model is given by a multilevel Anderson Hamiltonian. The weak-coupling theory at the particle-hole symmetric point is governed by a two-channel $S = 1$ Kondo model characterized by intrinsic channels asymmetry. Based on a conformal field theory approach we derived an effective Hamiltonian at a strong-coupling fixed point. The Hamiltonian capturing the low-energy physics of a two-stage Kondo screening represents the quantum impurity by a two-color local Fermi liquid. Using nonequilibrium (Keldysh) perturbation theory around the strong-coupling fixed point we analyze the transport properties of the model at finite temperature, Zeeman magnetic field, and source-drain voltage applied across the quantum dot. We compute the Fermi-liquid transport constants and discuss different universality classes associated with emergent symmetries.

DOI: [10.1103/PhysRevB.97.195403](https://doi.org/10.1103/PhysRevB.97.195403)**I. INTRODUCTION**

It is almost four decades since the seminal work of Nozières and Blandin (NB) [1] about the Kondo effect in *real* metals. The concept of the Kondo effect studied for impurity spin $S = 1/2$ interacting with a single orbital channel $\mathcal{K} = 1$ of conduction electrons [2–10] has been extended for arbitrary spin S and arbitrary number of channels \mathcal{K} [1]. A detailed classification of possible ground states corresponding to the underscreened $\mathcal{K} < 2S$, fully screened $\mathcal{K} = 2S$, and overscreened $\mathcal{K} > 2S$ Kondo effect has been given in Refs. [11–14]. Furthermore, it has been argued that in real metals the spin-1/2 single-channel Kondo effect is unlikely to be sufficient for the complete description of the physics of a magnetic impurity in a nonmagnetic host [15–22]. In many cases truncation of the impurity spectrum to one level is not possible and besides, there are several orbitals of conduction electrons which interact with the higher spin $S > 1/2$ of the localized magnetic impurity [23], giving rise to the phenomenon of multichannel Kondo screening [24,25]. In the fully screened case the conduction electrons completely screen the impurity spin to form a singlet ground state [26]. As a result, the low-energy physics is described by a local Fermi liquid (FL) theory [1,9]. In the underscreened Kondo effect there exist not enough conducting channels to provide complete screening [27,28]. Thus, there is a finite concentration of impurities with a residual spin contributing to the thermodynamic and transport properties. In contrast to the underscreened and fully screened cases, the physics of the overscreened Kondo effect is not described by the FL paradigm resulting in dramatic change of the thermodynamic and transport behavior [23].

The simplest realization of the multichannel fully screened Kondo effect is given by the model of a $S = 1$ localized impurity screened by two conduction electron channels. It

has been predicted [20] that in spite of the FL universality class of the model, the transport properties of such FL are highly nontrivial. In particular, the screening develops in two stages (see Fig. 1), resulting in nonmonotonic behavior of the transport coefficients (see review [20] for details).

The interest in the Kondo effect revived during the last two decades due to progress in the fabrication of nanostructures [29]. Usually in nanosized objects such as quantum dots (QDs), carbon nanotubes (CNTs), quantum point contacts (QPCs), etc., Kondo physics can be engineered by fine-tuning the external parameters (e.g., electric and magnetic fields) and develops in the presence of several different channels of the conduction electrons coupled to the impurity. Thus, it was timely [17,20,29–33] to uncover parallels between the Kondo physics in real metals and the Kondo effect in real quantum devices. The challenge of studying multichannel Kondo physics [1,24] was further revived in connection with possibilities to measure quantum transport in nanostructures experimentally [34–39] inspiring also many new theoretical suggestions [14,27,40–44].

Unlike the $S = 1/2$, $\mathcal{K} = 1$ Kondo effect (1CK), the two-channel $S = 1$ Kondo problem suffers from lack of universality for its observables [1]. The reason is that certain symmetries (e.g., conformal symmetry) present in 1CK are generally absent in the two-channel $S = 1$ model. This creates a major obstacle for constructing a complete theoretical description in the low-energy sector of the problem. Such a description should, in particular, account for a consistent treatment of the Kondo resonance [24] appearing in both orbital channels. The interplay between two resonance phenomena, being the central reason for the nonmonotonicity of transport coefficients [20], has remained a challenging problem for many years [27,43].

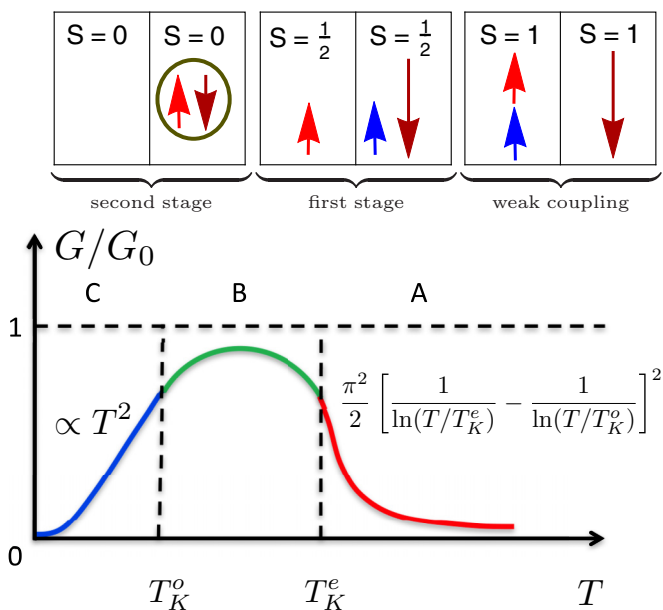


FIG. 1. Cartoon for nonmonotonic behavior of the differential conductance G/G_0 ($G_0 = 2e^2/h$ is the conductance quantum) as a function of temperature resulting from a two-stage Kondo effect. There are three characteristic regimes: (A) weak, (B) intermediate, and (C) strong coupling. Crossover energy scales T_K^e and T_K^o are defined in Sec. II. In the weak-coupling (A) regime the screening is absent (see top panel) and the transport coefficients are fully described by the perturbation theory [20]. In the intermediate regime (B), the Kondo impurity is partially screened (see the first stage at the top panel); the residual interaction of electrons with the underscreened spin is antiferromagnetic [1]. The description of the FL transport coefficients in the strong-coupling regime (C) at the second stage of the screening is the central result of the paper.

A sketch of the temperature dependence of the differential electric conductance is shown in Fig. 1. The most intriguing result is that the differential conductance vanishes at both high and low temperatures, demonstrating the existence of two characteristic energy scales (see detailed discussion below). These two energy scales are responsible for a two-stage screening of $S = 1$ impurity. Following [27,43] we will refer to the $S = 1, \mathcal{K} = 2$ Kondo phenomenon as the two-stage Kondo effect (2SK).

While both the weak (A) and intermediate (B) coupling regimes are well described by the perturbation theory [20], the most challenging and intriguing question is the study of the strong-coupling regime (C) where both scattering channels are close to the resonance scattering. Indeed, the theoretical understanding of the regime C (in and out of equilibrium) constitutes a long-standing problem that has remained open for more than a decade. Consequently, one would like to have a theory for the leading dependence of the electric current I and differential conductance $G = \partial I / \partial V$ on magnetic field (B), temperature (T), and voltage (V),

$$G(B, T, V)/G_0 = c_B B^2 + c_T (\pi T)^2 + c_V V^2.$$

Here $G_0 = 2e^2/h$ is unitary conductance. Computation of the parameters c_B , c_T , and c_V using a local FL theory, and to show how are these related, constitute the main message of this work.

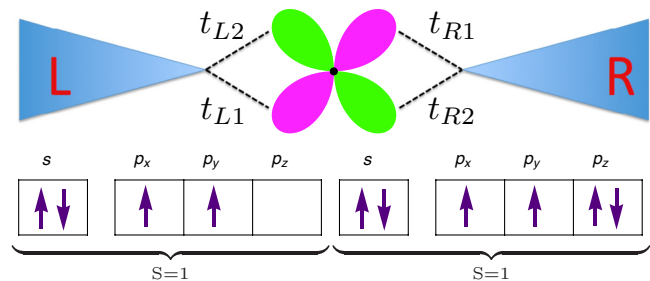


FIG. 2. Cartoon of some possible realizations of a multi-orbital Anderson model setup: two degenerate p orbitals (magenta and green) of a quantum dot are occupied by one electron each forming a triplet $S = 1$ state in accordance with the Hund's rule [48] (see lower panel). The third p orbital (not shown) is either empty or doubly occupied. Two limiting cases are important: (i) totally constructive interference $t_{L1} = t_{L2} = t_{R1} = t_{R2} = t$; and (ii) totally destructive interference $t_{L1} = t_{L2} = t_{R1} = t$, $t_{R2} = -t$. In addition, if $t_{L2} = t_{R2} = 0$, only one orbital is coupled to the leads, resulting in the 1CK model. If $t_{L2} = t_{R1} = 0$, each orbital is coupled to a “dedicated lead” and the net current through the dot is zero.

In this paper we offer a full-fledged theory of the two-stage Kondo model at small but finite temperature, magnetic field, and bias voltage to explain the charge transport (current, conductance) behavior in the strong-coupling regime of the 2SK effect. The paper is organized as follows. In Sec. II we discuss the multilevel Anderson impurity model along with different coupling regimes. The FL theory of the 2SK effect in the strong-coupling regime is addressed in Sec. III. We outline the current calculations which account for both elastic and inelastic effects using the nonequilibrium Keldysh formalism in Sec. IV. In Sec. V we summarize our results for the FL coefficients in different regimes controlled by external parameters and discuss the universal limits of the theory. Section VI is devoted to discussing perspectives and open questions. Mathematical details of our calculations are given in the Appendices.

II. MODEL

We consider a multilevel quantum dot sandwiched between two external leads α ($= L, R$) as shown in Fig. 2. The generic Hamiltonian is defined by the Anderson model

$$H = \sum_{k\alpha\sigma} (\xi_k + \varepsilon_\sigma^Z) c_{\alpha k\sigma}^\dagger c_{\alpha k\sigma} + \sum_{\alpha k i\sigma} t_{\alpha i} c_{\alpha k\sigma}^\dagger d_{i\sigma} + \text{H.c.} \\ + \sum_{i\sigma} (\varepsilon_i + \varepsilon_\sigma^Z) d_{i\sigma}^\dagger d_{i\sigma} + E_c \hat{N}^2 - \mathcal{J} \hat{S}^2, \quad (1)$$

where c_α stands for the Fermi-liquid quasiparticles of the source (L) and the drain (R) leads, $\xi_k = \varepsilon_k - \mu$ is the energy of conduction electrons with respect to the chemical potential μ , and spin $\sigma = \uparrow(+), \downarrow(-)$, and $\varepsilon_\sigma^Z = -\sigma B/2$. The operator $d_{i\sigma}$ describes electrons with spin σ in the i th orbital state of the quantum dot and $t_{\alpha i}$ are the tunneling matrix elements, as shown in Fig. 2. Here $\varepsilon_i + \varepsilon_\sigma^Z$ is the energy of the electron in the i th orbital level of the dot in the presence of a Zeeman field B , E_c is the charging energy (Hubbard interaction in the Coulomb blockade regime [40]), $\mathcal{J} \ll E_c$ is an exchange

integral accounting for Hund's rule [43], and $\hat{N} = \sum_{i\sigma} d_{i\sigma}^\dagger d_{i\sigma}$ is the total number of electrons in the dot. We assume that the dot is occupied by two electrons, and thus the expectation value of \hat{N} is $\bar{n}_d = 2$ and the total spin $S = 1$ (see Fig. 2). By applying a Schrieffer-Wolff (SW) transformation [45] to the Hamiltonian Eq. (1) we eliminated the charge fluctuations between two orbitals of the quantum dot and project out the effective Hamiltonian, written in the L - R basis, onto the spin-1 sector of the model [20,43]:

$$H_{\text{eff}} = \sum_{k\alpha\sigma} \xi_k c_{\alpha k\sigma}^\dagger c_{\alpha k\sigma} + \sum_{\alpha\alpha'} J_{\alpha\alpha'} [\mathbf{s}_{\alpha\alpha'} \cdot \mathbf{S}], \quad (2)$$

with $\alpha, \alpha' = L, R, B = 0$, and

$$\mathbf{s}_{\alpha\alpha'} = \frac{1}{2} \sum_{kk'\sigma_1\sigma_2} c_{\alpha k\sigma_1}^\dagger \boldsymbol{\tau}_{\sigma_1\sigma_2} c_{\alpha' k'\sigma_2}, \quad (3)$$

$$\mathbf{S} = \frac{1}{2} \sum_{i\sigma_1\sigma_2} d_{i\sigma_1}^\dagger \boldsymbol{\tau}_{\sigma_1\sigma_2} d_{i\sigma_2}, \quad (4)$$

$$J_{\alpha\alpha'} = \frac{2}{E_c} \begin{pmatrix} |t_{L1}|^2 + |t_{L2}|^2 & t_{L2}^* t_{R2} + t_{L1}^* t_{R1} \\ t_{L2} t_{R2}^* + t_{L1} t_{R1}^* & |t_{R2}|^2 + |t_{R1}|^2 \end{pmatrix}, \quad (5)$$

where we use the shorthand notation $\boldsymbol{\tau}_{\sigma_{ij}} \equiv \boldsymbol{\tau}_{\sigma_i\sigma_j}$ for the Pauli matrices.

The determinant of the matrix $J_{\alpha\alpha'}$ in Eq. (5) is nonzero provided that $t_{L2}t_{R1} \neq t_{L1}t_{R2}$. Therefore, one may assume without loss of generality that both eigenvalues of the matrix $J_{\alpha\alpha'}$ are nonzero and, hence, both scattering channels interact with the dot. There are, however, two important cases deserving an additional discussion. The first limiting case is achieved when two eigenvalues of $J_{\alpha\alpha'}$ are equal and the matrix $J_{\alpha\alpha'}$ is proportional to the unit matrix in any basis of electron states of the leads. As a result, the net current through impurity vanishes at any temperature, voltage, and magnetic field [43] (see Fig. 1, showing that the differential conductance vanishes when the symmetry between channels emerges). This is due to destructive interference between two paths [43] (Fig. 2) occurring when, e.g., $t_{L1} = t_{L2} = t_{R1} = t, t_{R2} = -t$. Precise calculations done later in the paper highlight the role of destructive interference effects and quantify how the current goes to zero in the vicinity of the symmetry point. The second limiting case is associated with constructive interference between two paths (Fig. 2) when $t_{L1} = t_{L2} = t_{R1} = t_{R2} = t$. In that case the determinant of the matrix $J_{\alpha\alpha'}$ in Eq. (5) and thus also one of the eigenvalues of $J_{\alpha\alpha'}$, is zero. As a result, the corresponding channel is completely decoupled from the impurity. The model then describes the underscreened $S = 1$ single-channel Kondo effect.

Applying the Glazman-Raikh rotation [46] $b_{e/o}^\dagger = (c_L^\dagger \pm c_R^\dagger)/\sqrt{2}$ to the effective Hamiltonian Eq. (2) we rewrite the Kondo Hamiltonian in the diagonal basis [47], introducing two coupling constants J_e, J_o ,

$$\mathcal{H}_{\text{eff}} = \sum_a (H_0^a + J_a \mathbf{s}_a \cdot \mathbf{S}). \quad (6)$$

In writing Eq. (6) we assigned the generalized index “ a ” to represent the even and odd channels ($a = e, o$). $H_0^a = \sum_{k\alpha\sigma} (\varepsilon_k - \mu) b_{\alpha k\sigma}^\dagger b_{\alpha k\sigma}$ is the noninteracting Hamiltonian of channel a in the rotated basis. The spin density operators in

the new basis are $\mathbf{s}_a = 1/2 \sum_{kk'\sigma_1\sigma_2} b_{\alpha k\sigma_1}^\dagger \boldsymbol{\tau}_{\sigma_1\sigma_2} b_{\alpha k'\sigma_2}$. For equal leads-dot coupling, the J_a are of the order of t^2/E_c . The interaction between even and odd channels is generated by the next nonvanishing order of Schrieffer-Wolff transformation

$$H_{eo} = -J_{eo} \mathbf{s}_e \cdot \mathbf{s}_o, \quad (7)$$

where J_{eo} is estimated as $J_{eo} \sim J_e J_o / \max[E_c, \mu]$. As a result this term is irrelevant in the weak-coupling regime. However, we note that the sign of J_{eo} is positive, indicating the ferromagnetic coupling between channels necessary for the complete screening of the $S = 1$ impurity [1] (see Fig. 1).

The Hamiltonian (6) describes the weak-coupling limit of the two-stage Kondo model. The coupling constants J_e and J_o flow to the strong-coupling fixed point [see details of the renormalization group (RG) analysis [7,8,49] in Appendix A1]. In the leading-log (one-loop RG) approximation, the two channels do not talk to each other. As a result, two effective energy scales emerge, referred to as Kondo temperatures, $T_K^a = D \exp[-1/(2N_F J_a)]$ (D is a bandwidth and N_F is the three-dimensional electron's density of states in the leads). These act as crossover energies, separating three regimes: the weak-coupling regime, $T \gg \max[T_K^a]$ (see Appendix A1); the intermediate regime, $\min[T_K^a] \ll T \ll \max[T_K^a]$ characterized by an incomplete screening (see Fig. 1) when one conduction channel (even) falls into a strong coupling regime while the other channel (odd) still remains at the weak coupling (see Appendix A2); and the strong-coupling regime, $T \ll \min[T_K^a]$. In the following section we discuss the description of the strong-coupling regime by a local Fermi-liquid paradigm.

III. FERMI-LIQUID HAMILTONIAN

The RG analysis of the Hamiltonian (6) (see Appendix A1 for details) shows that the 2SK model has a unique strong-coupling fixed point corresponding to complete screening of the impurity spin. This strong-coupling fixed point is of the FL-universality class. In order to account for the existence of two different Kondo couplings in the odd and even channels and the interchannel interaction, we conjecture that the strong-coupling fixed point Hamiltonian contains three leading irrelevant operators:

$$H = - \sum_{aa'} \lambda_{aa'} : \mathbf{s}_a(0) \cdot \mathbf{s}_{a'}(0) : , \quad (8)$$

with $\lambda_{ee} = \lambda_e$, $\lambda_{oo} = \lambda_o$, and $\lambda_{eo} = \lambda_{oe}$. The notation $:\dots:$ corresponds to a normal ordering where all divergences originating from bringing two spin currents \mathbf{s}_a close to each other are subtracted. The conjecture (8) is in the spirit of Affleck's ideas [24] of defining leading irrelevant operators of minimal operator dimension being simultaneously (i) local, (ii) independent of the impurity spin operator \mathbf{S} , (iii) rotationally invariant, and (iv) independent of the local charge density. We do not assume any additional [SO(3) or SU(2)] symmetry in the channel subspace except at the symmetry-protected point $\lambda_e = \lambda_o = \lambda_{eo} = \lambda$. At this symmetry point a new conservation law for the total spin current [24] emerges and the Hamiltonian reads as

$$H = -\lambda : \mathbf{S}(0) \cdot \mathbf{S}(0) : , \quad \mathbf{S} = \mathbf{s}_e + \mathbf{s}_o.$$

This symmetric point is obtained with the condition $J_e = J_o$ in H_{eff} [see Eq. (6)]. Under this condition, as has been discussed

in the previous section, the net current through the impurity is zero due to totally destructive interference. This symmetry protects the zero-current state at any temperature, magnetic, and/or electric field (see Fig. 2).

Applying the point-splitting procedure [24,50] to the Hamiltonian Eq. (8), we get $H = H_e + H_o + H_{eo}$ with

$$H_a = -\frac{3}{4}i\lambda_a \sum_{\sigma} \left[b_{a\sigma}^{\dagger} \frac{d}{dx} b_{a\sigma} - \left(\frac{d}{dx} b_{a\sigma}^{\dagger} \right) b_{a\sigma} \right] + \frac{3}{2}\lambda_a \rho_{a\uparrow} \rho_{a\downarrow},$$

$$H_{eo} = -\lambda_{eo} [\mathbf{s}_e(0) \cdot \mathbf{s}_o(0) + \mathbf{s}_o(0) \cdot \mathbf{s}_e(0)]. \quad (9)$$

The Hamiltonian Eq. (9) accounts for two copies of the $s = 1/2$ Kondo model at strong coupling with an additional ferromagnetic interaction between the channels providing complete screening at $T = 0$.

An alternative derivation of the strong-coupling Hamiltonian (9) can be obtained, following Refs. [51–53], with the most general form of the low-energy FL Hamiltonian. For the two-stage Kondo problem corresponding to the particle-hole symmetric limit of the two-orbital-level Anderson model, it is given by $H = H_0 + H_{\alpha} + H_{\phi} + H_{\Phi}$ with

$$H_0 = \sum_{a\sigma} \int_{\varepsilon} v(\varepsilon + \varepsilon_{\sigma}^Z) b_{a\sigma}^{\dagger} b_{a\sigma},$$

$$H_{\alpha} = -\sum_{a\sigma} \int_{\varepsilon_{1-2}} \frac{\alpha_a}{2\pi} (\varepsilon_1 + \varepsilon_2) b_{a\varepsilon_1\sigma}^{\dagger} b_{a\varepsilon_2\sigma},$$

$$H_{\phi} = \sum_a \int_{\varepsilon_{1-4}} \frac{\phi_a}{\pi v} : b_{a\varepsilon_1\uparrow}^{\dagger} b_{a\varepsilon_2\uparrow} b_{a\varepsilon_3\downarrow}^{\dagger} b_{a\varepsilon_4\downarrow} :,$$

$$H_{\Phi} = -\sum_{\sigma_{1-4}} \int_{\varepsilon_{1-4}} \frac{\Phi}{2\pi v} : b_{o\varepsilon_1\sigma_1}^{\dagger} \tau_{\sigma_{12}} b_{o\varepsilon_2\sigma_2} b_{e\varepsilon_3\sigma_3}^{\dagger} \tau_{\sigma_{34}} b_{e\varepsilon_4\sigma_4} :, \quad (10)$$

where $v = 1/(2\pi\hbar v_F)$ is the density of states per species for a one-dimensional channel. In Eq. (10) H_{α} describes energy-dependent elastic scattering [24]. The inter- and intrachannel quasiparticle interactions responsible for the inelastic effects are described by H_{Φ} and H_{ϕ} , respectively. The particle-hole symmetry of the problem forbids having any second generation of FL parameters [51] in Eq. (10). Therefore, the Hamiltonian Eq. (10) constitutes a minimal model for the description of a local Fermi liquid with two interacting resonance channels. The direct comparison of the above FL Hamiltonian with the strong-coupling Hamiltonian Eq. (9) provides the relation between the FL coefficients at particle-hole (PH) symmetry, namely, $\alpha_a = \phi_a$. The Kondo floating argument (see [51]) recovers this relation. As a result we have three independent FL coefficients α_e, α_o , and Φ which can be obtained from three independent measurements of the response functions. The FL coefficients in Eq. (10) are related to the leading irrelevant coupling parameter λ 's in Eq. (9) as

$$\alpha_a = \phi_a = \frac{3\lambda_a\pi}{2} \quad \text{and} \quad \Phi = \pi\lambda_{eo}. \quad (11)$$

The symmetry point $\lambda_e = \lambda_o = \lambda_{eo} = \lambda$ constrains $\alpha_e = \alpha_o = 3\Phi/2$ in the Hamiltonian Eq. (10).

To fix three independent FL parameters in (10) in terms of physical observables, three equations are needed. Two equations are provided by specifying the spin susceptibilities of two orthogonal channels. The remaining necessary equation can be obtained by considering the impurity contribution to

specific heat. It is proportional to an impurity-induced change in the total density of states per spin [23], $\nu_{a\sigma}^{\text{imp}}(\varepsilon) = \frac{1}{\pi} \partial_{\varepsilon} \delta_{\sigma}^a(\varepsilon)$, where $\delta_{\sigma}^a(\varepsilon)$ are energy-dependent scattering phases in odd and even channels (see the next section for more details)

$$\frac{C^{\text{imp}}}{C_{\text{bulk}}} = \frac{\sum_{a\sigma} \frac{1}{\pi} \partial_{\varepsilon} \delta_{\sigma}^a(\varepsilon)|_{\varepsilon=0}}{4\nu} = \frac{\alpha_e + \alpha_o}{2\pi\nu}. \quad (12)$$

The quantum impurity contributions to the spin susceptibilities of the odd and even channels (see details in [50]) are given by

$$\frac{\chi_e^{\text{imp}}}{\chi_{\text{bulk}}} = \frac{\alpha_e + \Phi/2}{\pi\nu}, \quad \frac{\chi_o^{\text{imp}}}{\chi_{\text{bulk}}} = \frac{\alpha_o + \Phi/2}{\pi\nu}. \quad (13)$$

Equations (12) and (13) fully determine three FL parameters α_e, α_o , and Φ in (10). Total spin susceptibility $\chi^{\text{imp}} = \chi_e^{\text{imp}} + \chi_o^{\text{imp}}$ together with the impurity specific heat (12) defines the Wilson ratio, $R = (\chi^{\text{imp}}/\chi_{\text{bulk}})/(C^{\text{imp}}/C_{\text{bulk}})$ [24,54], which measures the ratio of the total specific heat to the contribution originating from the spin degrees of freedom

$$R = 2 \left[\frac{\alpha_e + \alpha_o + \Phi}{\alpha_e + \alpha_o} \right] = 2 \left[1 + \frac{2}{3} \frac{\lambda_{eo}}{\lambda_e + \lambda_o} \right]. \quad (14)$$

For $\lambda_e = \lambda_o = \lambda_{eo}$, Eq. (14) reproduces the value $R = 8/3$ known for the two-channel, fully screened $S = 1$ Kondo model [55]. If, however, $\lambda_{eo} = 0$ we get $R = 2$, in agreement with the textbook result for two not necessarily identical but independent replicas of the single-channel Kondo model.

IV. CHARGE CURRENT

The current operator at position x is expressed in terms of first-quantized operators ψ attributed to the linear combinations of the Fermi operators in the leads

$$\hat{I}(x) = \frac{e\hbar}{2mi} \sum_{\sigma} [\psi_{\sigma}^{\dagger}(x) \partial_x \psi_{\sigma}(x) - \partial_x \psi_{\sigma}^{\dagger}(x) \psi_{\sigma}(x)]. \quad (15)$$

In the present case both types of quasiparticles $b_{a\sigma}$ ($a = e, o$) interact with the dot. Besides, both scattering phases (e/o) are close to their resonance value $\delta_{0,\sigma}^{e/o} = \pi/2$. This is in striking contrast to the single-channel Kondo model, where one of the eigenvalues of the 2×2 matrix of $J_{\alpha\alpha'}$ in Eq. (5) is zero, and hence the corresponding degree of freedom is completely decoupled in the interacting regime. For the sake of simplicity, we are going to consider the 2SK problem in the absence of an orbital magnetic field so that magnetic flux is zero. However, our results can be easily generalized for the case of finite orbital magnetic field. In this section we obtain an expression of charge current operator for the two-stage Kondo problem following the spirit of seminal works [51,56–59]. The principal idea behind the nonequilibrium calculations is to choose a basis of scattering states for the expansion of the current operator, Eq. (15). The scattering states in the first quantization representation are expressed as

$$\psi_{ek\sigma}(x) = \frac{1}{\sqrt{2}} \begin{cases} [e^{i(k_F+k)x} - S_{e,\sigma}(k)e^{-i(k_F+k)x}], & x < 0 \\ [e^{-i(k_F+k)x} - S_{e,\sigma}(k)e^{i(k_F+k)x}], & x > 0, \end{cases}$$

$$\psi_{ok\sigma}(x) = \frac{1}{\sqrt{2}} \begin{cases} [e^{i(k_F+k)x} - S_{o,\sigma}(k)e^{-i(k_F+k)x}], & x < 0 \\ [-e^{-i(k_F+k)x} + S_{o,\sigma}(k)e^{i(k_F+k)x}], & x > 0. \end{cases}$$

The phase shifts in even/odd channels are defined through the corresponding S matrix via the relation $S_{a,\sigma}(k) = e^{2i\delta_\sigma^a(\epsilon_k)}$. Proceeding to the second quantization, we project the operator $\psi_\sigma(x)$ over the eigenstates $\psi_{ek\sigma}(x)$ and $\psi_{ok\sigma}(x)$, choosing $x < 0$ far from the dot, to arrive at the expression

$$\psi_\sigma(x) = \frac{1}{\sqrt{2}} \sum_{k\sigma} \{ [e^{i(k_F+k)x} - S_{e,\sigma}(k)e^{-i(k_F+k)x}] b_{ek\sigma} + [e^{i(k_F+k)x} - S_{o,\sigma}(k)e^{-i(k_F+k)x}] b_{ok\sigma} \}. \quad (16)$$

Substituting Eq. (16) into Eq. (15) and using $b_{a\sigma}(x) = \sum_k b_{ak\sigma} e^{ikx}$ and $Sb_{a\sigma}(x) = \sum_k S(k)b_{ak\sigma} e^{ikx}$, we obtain an expression for the current for symmetrical dot-leads coupling,

$$\hat{I}(x) = \frac{e}{2h\nu} \sum_\sigma [b_{o\sigma}^\dagger(x)b_{e\sigma}(x) - b_{o\sigma}^\dagger(-x)Sb_{e\sigma}(-x) + \text{H.c.}], \quad (17)$$

where $S = S_o^*S_e$. There are two contributions to the charge current, coming from elastic and inelastic processes. The elastic effects are characterized by the energy-dependent phase shifts, and the inelastic ones are due to the interaction of Fermi-liquid quasi particles. In the following section we outline the elastic and inelastic current contribution of the two-stage Kondo model, Eq. (10).

A. Elastic current

We assume that the left and right scattering states are in thermal equilibrium at temperature $T_L = T_R = T$ and at the chemical potentials μ_R and $\mu_L = \mu_R + eV$. The population of states reads $2\langle b_{ak\sigma}^\dagger b_{ak'\sigma} \rangle = \delta_{kk'} [f_L(\epsilon_k) + f_R(\epsilon_k)]$ and $2\langle b_{ak\sigma}^\dagger b_{\bar{a}k'\sigma} \rangle = \delta_{kk'} [f_L(\epsilon_k) - f_R(\epsilon_k)] = \delta_{kk'} \Delta f(\epsilon_k)$ where $f_{L/R}(\epsilon_k) = f(\epsilon_k - \mu_{L/R})$ and $f(\epsilon_k) = (1 + \exp[\epsilon_k/T])^{-1}$ is the Fermi-distribution function. The zero temperature conductance in the absence of bias voltage is [20]

$$G(T=0, B \neq 0, V=0)/G_0 = B^2(\alpha_e - \alpha_o)^2.$$

The elastic current in the absence of Zeeman field B is the expectation value of the current operator, Eq. (17). Taking the expectation value of Eq. (17) reproduces the Landauer-Büttiker equation [60]

$$I_{\text{el}} = \frac{2e}{h} \int_{-\infty}^{\infty} d\epsilon T(\epsilon) \Delta f(\epsilon), \quad (18)$$

where the energy-dependent transmission coefficient, $T(\epsilon) = \frac{1}{2} \sum_\sigma \sin^2[\delta_\sigma^e(\epsilon) - \delta_\sigma^o(\epsilon)]$ and $\Delta f(\epsilon) = f_L(\epsilon) - f_R(\epsilon)$. Diagrammatically (see Refs. [24,50] for details), the elastic corrections to the current can be reabsorbed into a Taylor expansion for the energy-dependent phase shifts through the purely elastic contributions to quasiparticle self-energies [24]. That is, the scattering phase shifts can be read off [24] via the real part of the retarded self-energies $\Sigma_{a,\sigma}^R(\epsilon)$ (see Fig. 3) as

$$\delta_\sigma^a(\epsilon) = -\pi\nu \text{Re} \Sigma_{a,\sigma}^R(\epsilon) = \pi/2 + \alpha_a \epsilon. \quad (19)$$

The Kondo temperatures of the two channels in the strong-coupling limit are defined as

$$T_K^a = \frac{1}{\alpha_a}. \quad (20)$$

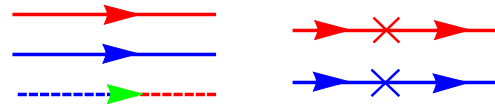


FIG. 3. Left panel: Feynman codex used for the representation of different Green's functions: blue (red) line [in the black and white print version the colors are different by intensity of gray (red is more intensive)] for the Green's function of even (odd) channel $G_{e(o)}$ and the mixed line for the mixed Green's function G_{eo} (see definition in Sec IV B 1). Right panel: two-particle elastic vertices for even and odd channels. Crosses denote energy-dependent scattering.

This definition is consistent with Nozieres-Blandin [1] and identical to that used in [50]; however, it differs by the coefficient $\pi/4$ from the spin-susceptibility based definition [53]. The elastic phase shifts in the presence of the finite Zeeman field B bears the form [20] [see schematic behavior of $\delta_\sigma^a(B)$ in Fig. 4]

$$\delta_\sigma^a(B) = \pi/2 - (\alpha_a + \phi_a + \Phi)\bar{\sigma} B/2. \quad (21)$$

Finally, we expand Eq. (18) up to second order in α_a to get the elastic contribution to the current [56,61],

$$\frac{I_{\text{el}}}{2e^2V/h} = \left[B^2 + \frac{(eV)^2}{12} + \frac{(\pi T)^2}{3} \right] (\alpha_e - \alpha_o)^2. \quad (22)$$

The B^2 elastic term is attributed to the Zeeman field in Eq. (1). Note that we do not consider the orbital effects assuming that the magnetic field is applied parallel to the plane of the electron gas. The expression, Eq. (22), remarkably highlights the absence of a linear response at $T=0$, $B=0$, due to the vanishing of conductance when both scattering phases achieve the resonance value $\pi/2$. The current is exactly zero at the symmetry point $\alpha_e = \alpha_o$ [20] due to the diagonal form of the S matrix characterized by two equal eigenvalues and therefore proportional to the unit matrix.

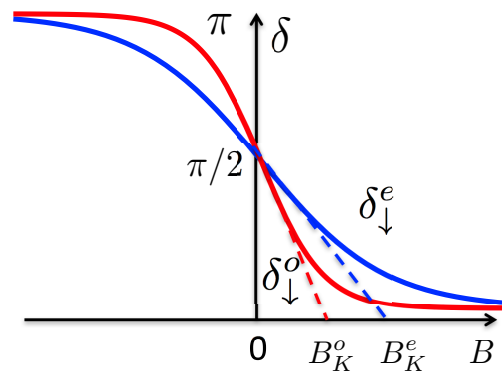


FIG. 4. Schematic behavior of the even (blue) and odd (red) scattering phases at $\sigma = \downarrow$ as a function of the Zeeman magnetic field. Both phases approach the resonance value $\pi/2$ at zero field. The tangential lines illustrate corresponding energy scales inversely proportional to the spin susceptibilities (13) in the even/odd channels, $B_K^a = \pi/(2\alpha_a + \Phi)$ [see also Eqs. (19)–(21)].

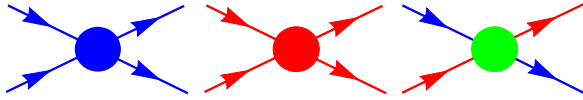


FIG. 5. Feynman diagrammatic codex used for the calculation of inelastic current. Blue (red) circle denotes the density-density intrachannel interaction in the even (odd) channel [see Eq. (10)]. Green circle denotes the interchannel spin-spin interaction Eq. (10).

B. Inelastic current

To calculate the inelastic contribution to the current we apply the perturbation theory using the Keldysh formalism [62],

$$\delta I_{\text{in}} = \langle T_C \hat{I}(t) e^{-i \int dt' H_{\text{int}}(t')} \rangle, \quad (23)$$

where $H_{\text{int}} = H_\phi + H_\Phi$ and C denotes the double-side $\eta = \pm$ Keldysh contour. Here T_C is the corresponding time-ordering operator. The average is performed with the Hamiltonian H_0 . The effects associated with the quadratic Hamiltonian H_α are already accounted in I_{el} . Therefore, to obtain the second-order correction to the inelastic current we proceed by considering $H_{\text{int}} = H_\phi + H_\Phi$, with the Feynman diagrammatic codex as shown in Fig. 5.

The perturbative expansion of Eq. (23) in $(B, T, eV) \ll T_K^0$ starts with the second-order contribution [24] and is illustrated by Feynman diagrams of four types (see Fig. 6). The type-1 and type-2 diagrams contain only one mixed Green's function (GF) (dashed line) proportional to $\Delta f(t) \sim eV$, where $\Delta f(t)$ is the Fourier transform of $\Delta f(\varepsilon)$ defined in Eq. (C3). Therefore, both diagrams fully define the linear-response contribution to the inelastic current, but also contain some nonlinear $\propto (eV)^3$ contributions. The type-1 diagram contains the mixed GF directly connected to the current vertex (Fig. 6) and can be expressed in terms of single-particle self-energies. The type-2 diagram contains the mixed GF completely detached from the current vertex and therefore cannot be absorbed into self-energies. We will refer to this topology of Feynman diagram as a vertex correction. Note, that the second-order Feynman

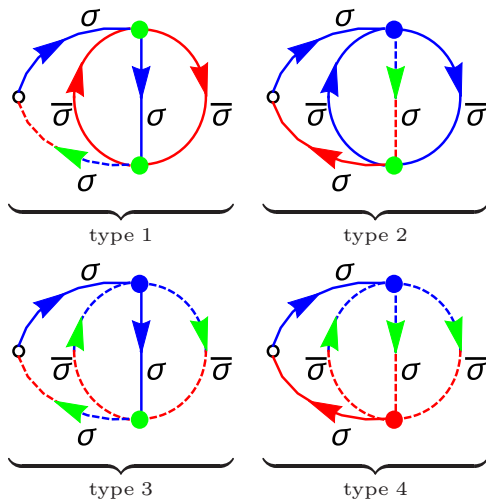


FIG. 6. Examples of four different types of Feynman diagrams contributing to the inelastic current. The open circle represents the current vertex. The other notations have been defined in Figs. 3 and 5.

diagrams containing two (and also four) mixed GFs are forbidden due to the PH symmetry of the problem. The type-3 and type-4 diagrams contain three mixed GFs and therefore contribute only to the nonlinear response being proportional to $(eV)^3$. The type-3 diagram, similarly to the type-1 diagram, can be absorbed into the single-particle self-energies. The type-4 diagram, similarly to the type-2 diagram, is contributing to the vertex corrections. This classification can be straightforwardly extended to higher order perturbation corrections for the current operator. Moreover, the diagrammatic series will have similar structure also for the Hamiltonians without particle-hole symmetry where more vertices are needed to account for different types of interactions. A similar classification can also be done for current-current (noise) correlation functions [63]. The mathematical details of the computation of the diagrammatic contribution of current correction diagrams type-1, type-2, type-3, and type-4 as shown in Fig. 6 proceed as follows.

1. Evaluation of type-1 diagram

The straightforward calculation of the Keldysh GFs at $x = 0$ takes the form (see Refs. [57,61] for details)

$$G_{aa}(k, \varepsilon) = \frac{1}{\varepsilon - \varepsilon_k} \tau_z + i\pi \begin{pmatrix} F_0 & F_0 + 1 \\ F_0 - 1 & F_0 \end{pmatrix} \delta(\varepsilon - \varepsilon_k),$$

$$G_{aa}(k, \varepsilon) = i\pi \begin{pmatrix} 1 & 1 \\ 1 & 1 \end{pmatrix} \Delta f(k, \varepsilon) \delta(\varepsilon - \varepsilon_k), \quad (24)$$

where $F_0 = f_L + f_R - 1$ and the Pauli matrix $\tau_z = \begin{pmatrix} 1 & 0 \\ 0 & -1 \end{pmatrix}$. The current contribution proportional to Φ^2 corresponding to the diagram of type 1 as shown in Fig. 6 is given by [57]

$$\delta I_{\text{int}}^{\Phi^2} = \frac{e}{v\hbar} \sum_{\eta_1, \eta_2} \eta_1 \eta_2 \mathcal{Y}_1^{\eta_1, \eta_2}, \quad (25)$$

with

$$\mathcal{Y}_1^{\eta_1, \eta_2} = \int \frac{d\varepsilon}{2\pi} [iS G_{ee}^{+\eta_1}(-x, \varepsilon) \Sigma^{\eta_1 \eta_2}(\varepsilon) G_{eo}^{\eta_2}(x, \varepsilon) + \text{c.c.}],$$

where $S = S_o^* S_e$, and $\eta_{1/2}$ are the Keldysh branch indices which take the value of + or -. The self-energy $\Sigma^{\eta_1 \eta_2}$ in real time is

$$\Sigma^{\eta_1 \eta_2}(t) = \left(\frac{\Phi}{\pi v^2} \right)^2 \sum_{k_1, k_2, k_3} G_{ee}^{\eta_1 \eta_2}(k_1, t) \times G_{ee}^{\eta_2 \eta_1}(k_2, -t) G_{ee}^{\eta_1 \eta_2}(k_3, t). \quad (26)$$

Using Eq. (24) we express the diagonal and mixed GFs in real space as

$$G_{aa}^{\eta_1 \eta_2}(\alpha x, \varepsilon) = i\pi v e^{i\alpha \varepsilon x / v_F} \left[F_0 + \begin{cases} \eta_1, & \text{if } \alpha = 1 \\ -\eta_2, & \text{if } \alpha = -1 \end{cases} \right],$$

$$G_{aa}^{\eta_1 \eta_2}(x, \varepsilon) = i\pi v e^{i\varepsilon x / v_F} \Delta f(\varepsilon). \quad (27)$$

The expression of corresponding GFs in real time is obtained by writing the Fourier transform of $[F_0(\varepsilon) \pm 1]$ as follows:

$$\int \frac{d\varepsilon}{2\pi} [F_0(\varepsilon) \pm 1] e^{-i\varepsilon t}$$

$$= \frac{i}{2\pi} \left[\pm \frac{\pi T}{\sinh(\pi T t)} (e^{-i\mu_L t} + e^{-i\mu_R t}) - 2 \frac{e^{\pm i D t}}{t} \right]. \quad (28)$$

Summing Eq. (25) over η_1 and η_2 using Eq. (27) results in two terms involving $\Sigma^{++} - \Sigma^{--}$ and $\Sigma^{-+} - \Sigma^{+-}$. The first term produces the contribution which is proportional to the model cutoff D , and is eliminated by introducing the counterterms in the Hamiltonian. In the rest of the calculation we consider only the contribution which remains finite for $D \rightarrow \infty$. As a result we get

$$\delta I_{\text{int}}^{\Phi^2} = \frac{2e\pi}{h} \int \frac{d\varepsilon}{2\pi} [\Sigma^{-+}(\varepsilon) - \Sigma^{+-}(\varepsilon)] i\pi v \Delta f(\varepsilon). \quad (29)$$

In Eq. (29) we used $\mathcal{S} + \mathcal{S}^* = 2 \cos(\delta_{0,\sigma}^e - \delta_{0,\sigma}^o) = 2$ with $\delta_{0,\sigma}^e = \delta_{0,\sigma}^o = \pi/2$. Fourier transformation of Eq. (29) into real time takes the form

$$\delta I_{\text{int}}^{\Phi^2} = \frac{2e\pi}{h} \int dt [\Sigma^{-+}(t) - \Sigma^{+-}(t)] i\pi v \Delta f(-t). \quad (30)$$

From Eq. (28) the required Green's functions in real time are

$$G_{aa}^{+-}(t) = -\pi v T \frac{\cos\left(\frac{eV}{2}t\right)}{\sinh(\pi T t)}, \quad (31)$$

$$G_{eo}(t) = i\pi v T \frac{\sin\left(\frac{eV}{2}t\right)}{\sinh(\pi T t)}. \quad (32)$$

The Green's function $G_{aa}^{-+}(t)$ is related with that of $G_{aa}^{+-}(t)$ by causality identity. The self-energies in Eq. (30) are accessible by using the above Green's functions Eqs. (31) and (32) in self-energy Eq. (26). Then Eq. (30) results in

$$\delta I_{\text{int}}^{\Phi^2} = \frac{2e\pi}{h} \left(\frac{\phi_e}{\pi v^2}\right)^2 2i(\pi v T)^4 \int dt \frac{\cos^3\left(\frac{eV}{2}t\right) \sin\left(\frac{eV}{2}t\right)}{\sinh^4(\pi T t)}. \quad (33)$$

The integral Eq. (33) is calculated in Appendix E. Hence the interaction correction to the current corresponding to the type-1 diagrams shown in Fig. 6 is

$$\frac{\delta I_{\text{type 1}}^{\Phi^2}}{2e^2 V/h} = [A_V^{(1)}(eV)^2 + A_T^{(1)}(\pi T)^2] \Phi^2, \quad (34)$$

where $A_V^{(1)} = 5/12$ and $A_T^{(1)} = 2/3$. Alternatively, the calculation of the integral Eq. (29) can proceed by scattering T -matrix formalism. The single-particle self-energy difference associated with the diagram of type 1 is expressed in terms of the inelastic T -matrix to obtain [20,61]

$$\Sigma^{-+}(\varepsilon) - \Sigma^{+-}(\varepsilon) = \frac{\Phi^2}{i\pi v} \left[\frac{3}{4}(eV)^2 + \varepsilon^2 + (\pi T)^2 \right]. \quad (35)$$

Using this self-energy difference and following the same way as we computed the elastic current in Appendix C, one easily gets the final expression for the current correction contributed by the diagram of type 1.

2. Evaluation of type-2 diagram

The diagrammatic contribution of the type-2 diagram shown in Fig. 6 is proportional to $\phi_e \Phi$ given by

$$\delta I_{\text{int}}^{\phi_e \Phi} = \frac{e}{v h} \mathcal{J} = \frac{e}{v h} \sum_{\eta_1, \eta_2} \eta_1 \eta_2 \mathcal{Y}_2^{\eta_1, \eta_2}, \quad (36)$$

with

$$\mathcal{Y}_2^{\eta_1, \eta_2} = \int \frac{d\varepsilon}{2\pi} [i \mathcal{S} G_{ee}^{+\eta_1}(-x, \varepsilon) \Lambda_1^{\eta_1 \eta_2}(\varepsilon) G_{oo}^{\eta_2 -}(x, \varepsilon) + \text{c.c.}].$$

The self-energy part Λ_1 in real time is expressed as

$$\Lambda_1^{\eta_1 \eta_2}(t) = \frac{\phi_e \Phi}{(\pi v^2)^2} \sum_{k_1, k_2, k_3} G_{ee}^{\eta_1 \eta_2}(k_1, t) \times G_{ee}^{\eta_2 \eta_1}(k_2, -t) G_{eo}^{\eta_1 \eta_2}(k_3, t). \quad (37)$$

Substituting Eq. (27) into Eq. (36) followed by the summation over Keldysh indices, we get

$$\mathcal{J} = 2i \mathcal{S} (\pi v)^2 \int dt [(F_0 + 1)(t) \Lambda_1^{-+}(-t) - (F_0 - 1)(t) \Lambda_1^{+-}(-t)] + \text{c.c.} \quad (38)$$

Let us define the Green's function as $G_{ee}^{+-/-+}(t) = G_{oo}^{+-/-+}(t) \equiv G^{+-/-+}(t)$. Then we write

$$i\pi v (F_0 \pm 1)(t) = G^{+-/-+}(t), \quad (39)$$

where $(F_0 \pm 1)(t)$ is a shorthand notation for the Fourier transform of $F_0(\varepsilon) \pm 1$ defined by (28). Hence, Eq. (38) takes the form

$$\mathcal{J} = 2\mathcal{S} \pi v \int dt [G^{+-}(t) \Lambda_1^{-+}(-t) - G^{-+}(t) \Lambda_1^{+-}(-t)] + \text{c.c.} \quad (40)$$

The self energies in Eq. (37) cast the compact form

$$\Lambda_1^{\eta_1 \eta_2}(-t) = \frac{\phi_e \Phi}{(\pi v^2)^2} G^{\eta_1 \eta_2}(-t) G^{\eta_2 \eta_1}(t) G_{eo}(-t). \quad (41)$$

Then the Eq. (40) becomes

$$\mathcal{J} = 4\mathcal{S} \pi v \frac{\phi_e \Phi}{(\pi v^2)^2} \int dt [G^{+-}(t)]^3 G_{eo}(t) + \text{c.c.} \quad (42)$$

Using the explicit expressions of the Green's functions Eqs. (31) and (32) together with Eq. (42) leads to

$$\mathcal{J} = -4i(\pi v)^2 \mathcal{S} T (\pi v T)^3 \frac{\phi_e \Phi}{(\pi v^2)^2} \times \int dt \frac{\cos^3\left(\frac{eV}{2}t\right) \sin\left(\frac{eV}{2}t\right)}{\sinh^4(\pi T t)}. \quad (43)$$

Substituting the value of integral given by Eq. (E9) into Eq. (43) and using Eq. (36) we get

$$\frac{\delta I_{\text{type 2}}^{\phi_e \Phi}}{2e^2 V/h} = [A_V^{(2)}(eV)^2 + A_T^{(2)}(\pi T)^2] \phi_e \Phi, \quad (44)$$

where $A_V^{(2)} = -5/6$ and $A_T^{(2)} = -4/3$.

3. Evaluation of type-3 diagram

Here we calculate the contribution to the current given by the diagram which consists of the self energy with two mixed Green's functions and one diagonal Green's function (type-3 diagram). The diagram shown in Fig. 6 describes correction proportional to $\phi_e \Phi$ and is given by

$$\delta I_{\text{int}}^{\phi_e \Phi} = \frac{e}{v h} \sum_{\eta_1, \eta_2} \eta_1 \eta_2 \mathcal{Y}_3^{\eta_1, \eta_2}, \quad (45)$$

with

$$\mathcal{Y}_3^{\eta_1, \eta_2} = \int \frac{d\varepsilon}{2\pi} [iS G_{ee}^{+\eta_1}(-x, \varepsilon) \Lambda_2^{\eta_1 \eta_2}(\varepsilon) G_{eo}^{\eta_2 -}(x, \varepsilon) + \text{c.c.}].$$

The self-energy $\Lambda_2^{\eta_1 \eta_2}$ in real time is

$$\begin{aligned} \Lambda_2^{\eta_1 \eta_2}(t) &= \frac{\phi_e \Phi}{(\pi v^2)^2} \sum_{k_1, k_2, k_3} G_{eo}^{\eta_1 \eta_2}(k_1, t) \\ &\quad \times G_{oe}^{\eta_2 \eta_1}(k_2, -t) G_{ee}^{\eta_1 \eta_2}(k_3, t). \end{aligned} \quad (46)$$

Summing Eq. (45) over η_1 and η_2 using Eq. (27), we get

$$\begin{aligned} \delta I_{\text{int}}^{\phi_e \Phi} &= -\frac{e}{v h} \times \pi v S \int \frac{d\varepsilon}{2\pi} (\Lambda_2^{+-}(\varepsilon) \\ &\quad - \Lambda_2^{+ -}(\varepsilon)) i \pi v \Delta f(\varepsilon) + \text{c.c.} \end{aligned} \quad (47)$$

The Fourier transformation of Eq. (47) into real time gives

$$\begin{aligned} \delta I_{\text{int}}^{\phi_e \Phi} &= -\frac{e}{v h} \times \pi v S \int dt (\Lambda_2^{-+}(t) \\ &\quad - \Lambda_2^{+-}(t)) i \pi v \Delta f(-t) + \text{c.c.} \end{aligned} \quad (48)$$

Using the expressions of Green's functions in real time Eq. (31) and Eq. (32) allows to bring the interaction correction to the current Eq. (48) to a compact form

$$\delta I_{\text{int}}^{\phi_e \Phi} = \frac{2e\pi}{h} \times 2i(\pi v T)^4 \frac{\phi_e \Phi}{(\pi v^2)^2} \int dt \frac{\cos\left(\frac{eV}{2}t\right) \sin^3\left(\frac{eV}{2}t\right)}{\sinh^4(\pi T t)}. \quad (49)$$

Substituting Eq. (E12) into Eq. (49) we get

$$\frac{\delta I_{\text{type 3}}^{\phi_e \Phi}}{2e^2 V/h} = [A_V^{(3)}(eV)^2 + A_T^{(3)}(\pi T)^2] \phi_e \Phi,$$

where $A_V^{(3)} = -1/4$ and $A_T^{(3)} = 0$.

4. Evaluation of type-4 diagram

In this section we calculate the diagrammatic contribution of the $\phi_e \phi_o$ current diagrams (type-4 diagram) shown in Fig. 6. Similar to the type-2 diagram calculation, the current correction reads

$$\delta I_{\text{int}}^{\phi_e \phi_o} = \frac{e}{v h} \mathcal{L} = \frac{e}{v h} \sum_{\eta_1, \eta_2} \eta_1 \eta_2 \mathcal{Y}_4^{\eta_1, \eta_2}, \quad (50)$$

with

$$\mathcal{Y}_4^{\eta_1, \eta_2} = \int \frac{d\varepsilon}{2\pi} [iS G_{ee}^{+\eta_1}(-x, \varepsilon) \Lambda_3^{\eta_1 \eta_2}(\varepsilon) G_{oo}^{\eta_2 -}(x, \varepsilon) + \text{c.c.}]. \quad (51)$$

The self-energy part $\Lambda_3^{\eta_1 \eta_2}$ is given by the expression

$$\begin{aligned} \Lambda_3^{\eta_1 \eta_2}(t) &= \frac{\phi_e \phi_o}{(\pi v^2)^2} \sum_{k_1, k_2, k_3} G_{oe}^{\eta_1 \eta_2}(k_1, t) \\ &\quad \times G_{eo}^{\eta_2 \eta_1}(k_2, -t) G_{eo}^{\eta_1 \eta_2}(k_3, t). \end{aligned} \quad (52)$$

Substituting Eq. (27) into Eq. (51) followed by the summation over Keldysh indices, we get

$$\begin{aligned} \mathcal{L} &= 2iS(\pi v)^2 \int dt [(F_0 + 1)(t) \Lambda_3^{-+}(-t) \\ &\quad - (F_0 - 1)(t) \Lambda_3^{+-}(-t)] + \text{c.c.} \end{aligned} \quad (53)$$

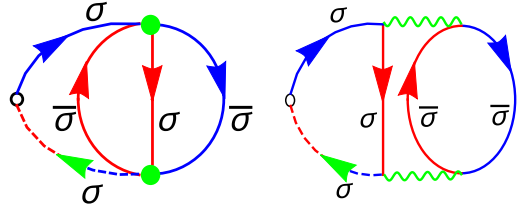


FIG. 7. The Φ^2 type-1 diagram (left panel) and the corresponding diagram with the splitting of local Φ vertices (right panel). In the diagram the upper Φ vertex contains the Pauli matrices product $\tau_{\sigma\bar{\sigma}} \tau_{\bar{\sigma}\sigma} = 2$. Similarly the lower Φ vertex contains the product of $\tau_{\bar{\sigma}\sigma} \tau_{\sigma\bar{\sigma}} = 2$. There are an even number of fermionic loops (two) and hence no extra negative sign occurs due to the fermionic loop. Each Φ vertex has the renormalization factor of $-\frac{1}{2}$. Hence the overall weight factor of this diagram is $\frac{1}{4} \times 4$ as will be seen in Figs. 11 and 12.

Plugging Eq. (39) into Eq. (53) results in

$$\mathcal{L} = 2S\pi v \int dt [G^{+-}(t) \Lambda_3^{-+}(-t) - G^{-+}(t) \Lambda_3^{+-}(-t)] + \text{c.c.} \quad (54)$$

The self-energy Eq. (54) takes the form

$$\Lambda_3^{-+}(-t) = \frac{\phi_e \phi_o}{(\pi v^2)^2} [G_{eo}(t)]^3 = \Lambda_3^{+-}(-t). \quad (55)$$

Hence combining Eqs. (31) and (32) we bring the required integral Eq. (54) to the form

$$\mathcal{L} = -\frac{\phi_e \phi_o}{(\pi v^2)^2} 4iS\pi v (\pi v T)^4 \int dt \frac{\cos\left(\frac{eV}{2}t\right) \sin^3\left(\frac{eV}{2}t\right)}{\sinh^4(\pi T t)} + \text{c.c.} \quad (56)$$

The integral in Eq. (56) is given by Eq. (E12). Hence plugging in Eq. (56) into Eq. (50) we obtain the current correction:

$$\frac{\delta I_{\text{type 4}}^{\phi_e \phi_o}}{2e^2 V/h} = [A_V^{(4)}(eV)^2 + A_T^{(4)}(\pi T)^2] \phi_e \phi_o, \quad (57)$$

where $A_V^{(4)} = 1/2$ and $A_T^{(4)} = 0$.

As we discussed above, all the current diagrams are of the form of type 1, type 2, type 3, and type 4. However, the same type of diagrams may contain different numbers of fermionic loops and also different spin combinations. In addition, there is the renormalization factor of $-\frac{1}{2}$ in H_Φ , which has to be accounted for the diagrams containing at least one Φ vertex. The same type of diagrams containing at least one Φ vertex with different spin combination have the different weight factor because of the product of the Pauli matrices in H_Φ . Each fermionic loop in the diagrams results in an extra (-1) multiplier in the corresponding weight factor. These facts will be accounted for by assigning the weight to the given current diagram (e.g., as shown in Figs. 7–9). However, in these equations proper weight factors which emerge from (i) the number of closed fermionic loops, (ii) SU(2) algebra of the Pauli matrices, and (iii) additional factors originating from the definition of the FL constants in the Hamiltonian (the extra factor of $-1/2$ in H_Φ) are still missing and are

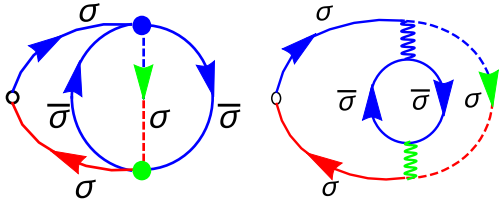


FIG. 8. The $\phi_e\Phi$ type-2 current correction diagram (left panel) and the corresponding diagram with the splitting of local Φ vertices (right panel). In the diagram the Φ vertex contains the Pauli matrices product $\tau_{\sigma\sigma}\tau_{\bar{\sigma}\bar{\sigma}} = -1$. There is an even number of fermionic loops (two) and hence no extra negative sign occurs due to the fermionic loop. The Φ vertex has the renormalization factor of $-\frac{1}{2}$. Hence the overall weight factor of this diagram is $-\frac{1}{2}(-1)$ as will be seen in Figs. 11 and 12.

accounted for separately. As a result, our final expression for the second-order perturbative interaction corrections to the current is given by (see Appendix D)

$$\begin{aligned} \frac{\delta I_{\text{in}}}{2e^2V/h} = & \left[\frac{2}{3}(\phi_e^2 + \phi_o^2) + 3\Phi^2 - 2(\phi_e + \phi_o)\Phi \right] (\pi T)^2 \\ & + \left[\frac{5}{12}(\phi_e^2 + \phi_o^2) + 3\Phi^2 - 2(\phi_e + \phi_o)\Phi \right. \\ & \left. + \frac{1}{2}\phi_e\phi_o \right] (eV)^2. \end{aligned} \quad (58)$$

The first term $\propto(\pi T)^2$ in Eq. (58) is the linear response result given by the type-1 and type-2 diagrams. The second term (surviving also at $T = 0$) is the nonlinear response contribution arising from all type 1–4 diagrams. The inelastic current Eq. (58) vanishes at the symmetry point. Moreover the linear response and the nonlinear response contributions vanish at the symmetry point independently. Also the elastic and inelastic currents approach zero separately when the system is fine-tuned to the symmetry point. These properties will be reproduced in arbitrary order of perturbation theory.

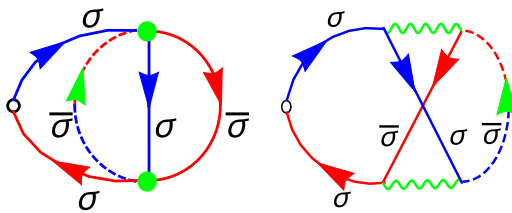


FIG. 9. The Φ^2 type-2 current correction diagram (left panel) and the corresponding diagram with the splitting of local Φ vertices (right panel). In the diagram the upper Φ vertex contains the Pauli matrices product $\tau_{\sigma\sigma}\tau_{\bar{\sigma}\bar{\sigma}} = -1$. Similarly the lower Φ vertex contains the product of $\tau_{\bar{\sigma}\bar{\sigma}}\tau_{\sigma\sigma} = 2$. There is one fermionic loop and one Cooperon-type (in contrast to Fig. 8) product of two Green's functions. Each Φ vertex has the renormalization factor of $-\frac{1}{2}$. Hence the overall weight factor of this diagram is $\frac{1}{4}(-2)$ as will be seen in Figs. 11 and 12.

V. TRANSPORT PROPERTIES

The total current consists of the sum of elastic and inelastic parts which upon using the FL identity $\alpha_a = \phi_a$ takes the form

$$\begin{aligned} \frac{\delta I}{2e^2V/h} = & [(\pi T)^2 + (eV)^2]3\left(\Phi - \frac{2}{3}\alpha_e\right)\left(\Phi - \frac{2}{3}\alpha_o\right) \\ & + \left[B^2 + (\pi T)^2 + \frac{1}{2}(eV)^2 \right] (\alpha_e - \alpha_o)^2. \end{aligned} \quad (59)$$

This Eq. (59) constitutes the main result of this work where the second term describes the universal behavior [20] scaled with $(1/T_K^e - 1/T_K^o)^2$, while the first one, containing an extra dependence on the ratio T_K^o/T_K^e accounts for the nonuniversality associated with the lack of conformal symmetry away from the symmetry-protected points. Equation (59) demonstrates the magnetic field B , temperature T , and voltage V behavior of the charge current characteristic for the Fermi-liquid systems. Therefore, following [50] we introduce the general FL constants as follows:

$$\frac{1}{G_0} \frac{\partial I}{\partial V} = c_B B^2 + c_T (\pi T)^2 + c_V (eV)^2. \quad (60)$$

$$\frac{c_T}{c_B} = 1 + 3\mathcal{F}, \quad \frac{c_V}{c_B} = \frac{3}{2} + 9\mathcal{F}. \quad (61)$$

Here the parameter

$$\mathcal{F} = \frac{(\Phi - \frac{2}{3}\alpha_e)(\Phi - \frac{2}{3}\alpha_o)}{(\alpha_e - \alpha_o)^2} = \frac{4(\lambda_{eo} - \lambda_e)(\lambda_{eo} - \lambda_o)}{9(\lambda_e - \lambda_o)^2}. \quad (62)$$

The parameter \mathcal{F} vanishes in the limit of strong asymmetry, $\lambda_{eo} \ll \lambda_e \ll \lambda_o$, in which the ratios

$$c_T/c_B|_{\lambda_{eo} \ll \lambda_e \ll \lambda_o} = 1, \quad c_V/c_B|_{\lambda_{eo} \ll \lambda_e \ll \lambda_o} = 3/2 \quad (63)$$

correspond to the universality class of the single-channel Kondo model [17,20].

On the other hand, near the symmetry point $\lambda_e = \lambda_o = \lambda_{eo}$, the function \mathcal{F} evidently depends sensitively on the precise manner in which the symmetry point is approached. In fact, *a priori* it appears unclear whether \mathcal{F} even reaches a well-defined value at this point. To clarify this, additional information on the parameters λ_e , λ_o , and λ_{eo} is required.

In full generality, the three parameters λ_e , λ_o , and λ_{eo} of the FL theory are independent from each other. Nonetheless, we are considering here a specific Hamiltonian Eq. (6) with only two independent parameters J_e and J_o , which implies that λ_{eo} is in fact a function of λ_e and λ_o . Although the corresponding functional form is not known, it can be deduced in the vicinity of the symmetric point $\lambda_e = \lambda_o = \lambda_{eo}$ from the following argument: the obvious $e \leftrightarrow o$ symmetry imposes that the Wilson ratio $R = 8/3$ is an extremum at the symmetric point (see Fig. 10), or in other words, that its derivative with respect to the channel imbalance ratio λ_o/λ_e vanishes. The only expression compatible with this requirement and the $e \leftrightarrow o$ symmetry is $\lambda_{eo} = (\lambda_e + \lambda_o)/2$, valid in the immediate vicinity of the symmetric point. Inserting this dependence into Eq. (62) predicts $\lim_{\lambda_e \rightarrow \lambda_o} \mathcal{F} = -1/9$ at the symmetric point, and

$$c_T/c_B|_{\lambda_{eo}=\lambda_e=\lambda_o} = 2/3, \quad c_V/c_B|_{\lambda_{eo}=\lambda_e=\lambda_o} = 1/2. \quad (64)$$

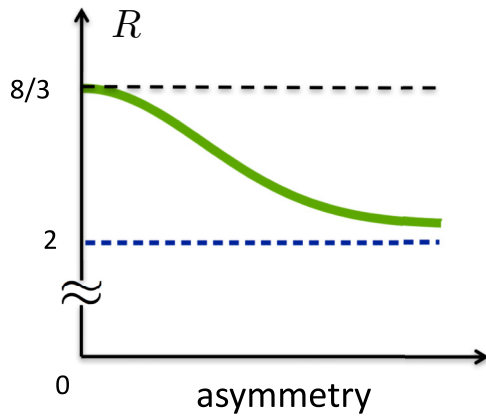


FIG. 10. Cartoon sketching the evolution of the Wilson ratio as a function of increasing “asymmetry,” meaning that the ratios λ_e/λ_o and λ_{eo}/λ_e both decrease from 1 at the left to 0 at the right. When $\lambda_e = \lambda_o = \lambda_{eo}$, meaning that the even and odd Kondo temperatures coincide, the total spin current is conserved [24] and $R = 8/3$ [55]. In the limit of the extremely (exponentially) strong channel asymmetry of the 2SK model, the C regime shown in Fig. 1 shrinks to zero. As a result, the 1CK universality class appears and the Wilson ratio is $R = 2$ [55]. The behavior of the Wilson ratio between these two limits is presumably monotonic, since the 2SK model has no other strong-coupling fixed points.

To summarize, under the assumption that the Wilson ratio is maximal at the symmetry point, we have arrived at the following conclusion: as the degree of asymmetry is reduced, i.e., the ratios λ_e/λ_o and λ_{eo}/λ_e increased from 0 to 1, the ratios of Fermi-liquid coefficients c_T/c_B and c_V/c_B decrease from the maximal values of Eq. (63), to the minimal values of Eq. (64), characteristic of the 1CK and 2SK fixed points, respectively.

VI. DISCUSSION

We constructed a Fermi-liquid theory of a two-channel, two-stage Kondo model when both scattering channels are close to the resonance. This theory completely describes the transport in the in- and out-of-equilibrium situations of the 2SK model. The elastic and inelastic contributions to the charge current through the 2SK model have been calculated using the full-fledged nonequilibrium Keldysh formalism for the arbitrary relation between two Kondo energy scales. While computing the current correction, we performed the full classification of the Feynman diagrams for the many-body perturbation theory on the Keldysh contour. We demonstrated the cancellation of the charge current at the symmetry-protected point. The linear response and beyond linear response contributions to the current vanish separately at the symmetry point. Moreover, the independent cancellation of the elastic and inelastic currents at the symmetry-protected point was verified. The theoretical method developed in the paper provides a tool for both quantitative and qualitative description of charge transport in the framework of the two-stage Kondo problem. In particular, the two ratios of FL constants, c_T/c_B and c_V/c_B , quantify the “amount” of interaction between two channels. The interaction is strongest at the symmetry-protected point

due to strong coupling of the channels. The interaction is weakest at the single-channel Kondo limit where the odd channel is completely decoupled from the even channel. While we illustrated the general theory of two resonance scattering channels by the two-stage Kondo problem, the formalism discussed in the paper is applicable for a broad class of models describing quantum transport through nanostructures [64–66] and the behavior of strongly correlated systems [67].

As an outlook, the approach presented in this paper can be applied to the calculation of current-current correlation functions (charge noise) of the 2SK problem and, by computing higher cumulants of the current, to studying the full-counting statistics [68,69]. It is straightforward to extend the presented ideas for generic Anderson-type models away from the particle-hole symmetric point [70–72], and generalize it for the $SU(N)$ Kondo impurity [61] and multiterminal (multistage) as well as multidot setup. The general method developed in the paper is not limited by its application to charge transport through quantum impurity—it can be equally applied to a detailed description of the thermoelectric phenomena on the nanoscale [61].

ACKNOWLEDGMENTS

We thank Ian Affleck, Igor Aleiner, Boris Altshuler, Natan Andrei, Andrey Chubukov, Piers Coleman, Leonid Glazman, Karsten Flensberg, Dmitry Maslov, Konstantin Matveev, Yigal Meir, Alexander Nersesyan, Yuval Oreg, Nikolay Prokof’ev, and Subir Sachdev for fruitful discussions. We are grateful to Seung-Sup Lee for discussions and sharing his preliminary results on a numerical study of multilevel Anderson and Kondo impurity models. This work was finalized at the Aspen Center for Physics, which was supported by National Science Foundation Grant No. PHY-1607611 and was partially supported (M.N.K.) by a grant from the Simons Foundation. J.v.D. was supported by the Nanosystems Initiative Munich. D.B.K. and M.N.K. appreciate the hospitality of the Physics Department, Arnold Sommerfeld Center for Theoretical Physics and Center for NanoScience, Ludwig-Maximilians-Universität München, where part of this work has been performed.

APPENDIX A: OVERVIEW OF FLOW FROM WEAK TO STRONG COUPLING

1. Weak-coupling regime

We assume that at sufficiently high temperatures (a precise definition of this condition is given below) the even and odd channels do not talk to each other. As a consequence, we renormalize the coupling between channels and impurity spins ignoring the cross-channel interaction. Performing Anderson’s poor man’s scaling procedure [49] on the even and odd channels independently we obtain the system of two decoupled RG equations:

$$\frac{dJ_e}{d\Lambda} = 2N_F J_e^2, \quad \frac{dJ_o}{d\Lambda} = 2N_F J_o^2, \quad (\text{A1})$$

where N_F is the 3D density of states in the leads. The parameter $\Lambda = \ln(\frac{D}{\epsilon})$ depends on the ultraviolet cutoff of the problem (conduction bandwidth D). Note that the RG equations (A1) are decoupled only in one-loop approximation

(equivalent to a summation of so-called parquet diagrams). The solution of these RG equations defines two characteristic energy scales, namely, $T_K^a = D \exp[-1/(2N_F J_a)]$, which are the Kondo temperatures in the even and odd channels, respectively. The second-loop corrections to RG couple the equations, generating the cross term $\propto -J_{eo} \mathbf{s}_e \cdot \mathbf{s}_o$ with $J_{eo} \sim N_F J_e J_o$. This emergent term flows under RG and becomes one of the leading irrelevant operators of the strong-coupling fixed point [the others are $\mathbf{s}_e \cdot \mathbf{s}_e$ and $\mathbf{s}_o \cdot \mathbf{s}_o$; see Eq. (8)]. In addition, the second-loop corrections to RG lead to a renormalization of the preexponential factor in the definition of the Kondo temperatures.

Summarizing, we see that the $S = 1$, $\mathcal{K} = 2$ fully screened Kondo model has a unique strong-coupling fixed point, where couplings J_e and J_o diverge in the RG flow. This strong-coupling fixed point falls into the FL universality class. The weak-coupling regime is therefore defined as $(B, T, eV) \gg (T_K^e, T_K^o)$. Since the interaction between the even channel and local impurity spin corresponds to the maximal eigenvalue of the matrix Eq. (5), we will assume below that the condition $T_K^e \geq T_K^o$ holds for any given B , T , and eV and, we thus define $T_K^{\min} = T_K^o$. The differential conductance decreases monotonically with increasing temperature in the weak-coupling regime (see Fig. 1) being fully described by the perturbation theory [20] in $[1/\ln(T/T_K^e), 1/\ln(T/T_K^o)] \ll 1$.

2. Intermediate-coupling regime

Next we consider the intermediate-coupling regime $T_K^o \leq (B, T, eV) \leq T_K^e$ depicted as the characteristic hump in Fig. 1. Since the solution of one-loop RG equations (A1) is given with logarithmic accuracy, we assume without loss of generality that T_K^e and T_K^o are of the same order of magnitude unless a very strong (exponential) channel asymmetry is considered. Therefore, the ‘‘hump regime’’ is typically very small and the hump does not have enough room to be formed. The intermediate regime is characterized by an incomplete screening (see Fig. 1) when one conduction channel (even) falls into a strong-coupling regime while the other channel (odd) still remains at the weak coupling. Then the strong-coupling Hamiltonian for the even channel is derived along the lines of the Affleck-Ludwig paper, Ref. [24], and is given by

$$H_{\text{even}} = H_0^e + \frac{3}{2} \lambda_e \rho_{e\uparrow} \rho_{e\downarrow} - \frac{3}{4v_F} \lambda_e \sum_{kk'\sigma} (\varepsilon_k + \varepsilon'_k) b_{ek\sigma}^\dagger b_{ek'\sigma}, \quad (\text{A2})$$

where the b operators describe Fermi-liquid excitations, $\rho_{e\sigma}(x=0) = \sum_{kk'} b_{ek\sigma}^\dagger b_{ek'\sigma}$, and $\lambda_e \propto 1/T_K^e$ is the leading irrelevant coupling constant [24].

The weak-coupling part of the remaining Hamiltonian is described by a $s_{\text{imp}} = 1/2$ Kondo-impurity Hamiltonian $H_{\text{odd}} = J_o \mathbf{s}_o \cdot \mathbf{s}_{\text{imp}}$. Here we have already taken into account that the impurity spin is partially screened by the even channel during the first stage process of the Kondo effect. We remind one that the coupling between the even and odd channels is facilitated by a *ferromagnetic* interaction [27] which emerges, being however irrelevant in the intermediate coupling regime where complete screening is not yet achieved. Thus, the differential conductance does reach a maximum $G/G_0 \approx 1$

with a characteristic hump [17,27,43] at the intermediate coupling regime. Corresponding corrections (deviation of the conductance at the top of the hump from the unitary limit $G_0 = 2e^2/h$) can be calculated with logarithmic accuracy $|\delta G/G_0| \propto 1/\ln^2(T_K^e/T_K^o)$ [1,49] (see also review [20] and [43] for details).

APPENDIX B: COUNTERTERMS

We proceed with the calculation of the corrections to the current by eliminating the dependence on the cutoff parameter D by adding the counterterms in the Hamiltonian [24,57]

$$H_c = -\frac{1}{2\pi v} \sum_a \sum_{kk'\sigma} (\delta\alpha_a + \delta\Phi)(\varepsilon_k + \varepsilon'_k) : b_{ak\sigma}^\dagger b_{ak'\sigma} : , \quad (\text{B1})$$

so that we consider only the contribution which remains finite for $D \rightarrow \infty$. Equation (B1) corresponds to the renormalization of the leading irrelevant coupling constant α_a such that $\alpha_a \rightarrow \alpha_a + \delta\alpha_a + \delta\Phi$ with

$$\delta\alpha_a = -\alpha_a \phi_a \frac{6D}{\pi} \log\left(\frac{4}{3}\right), \quad (\text{B2})$$

$$\delta\Phi = -\Phi^2 \frac{9D}{\pi} \log\left(\frac{4}{3}\right). \quad (\text{B3})$$

During the calculation of the interaction correction we neglected those terms which produce the contribution proportional to the cutoff D [for example, $\propto \int \frac{d\varepsilon}{2\pi} [\Sigma^{++}(\varepsilon) - \Sigma^{--}(\varepsilon)] i\pi v \Delta f(\varepsilon)$]. This renormalization of the leading irrelevant coupling constant Eq. (B1) exactly cancels these terms.

APPENDIX C: ELASTIC CURRENT

To get the elastic current Eq. (22), we start from the Landauer-Büttiker formula Eq. (18),

$$I_{\text{el}} = \frac{2e}{h} \int_{-\infty}^{\infty} d\varepsilon T(\varepsilon) \Delta f(\varepsilon), \quad (\text{C1})$$

where the energy-dependent transmission coefficient, $T(\varepsilon) = \frac{1}{2} \sum_{\sigma} \sin^2[\delta_{\sigma}^e(\varepsilon) - \delta_{\sigma}^o(\varepsilon)]$ and $\Delta f(\varepsilon) = f_L(\varepsilon) - f_R(\varepsilon)$. Taylor expanding the phase shifts to the first order in energy and retaining only up to second order in energy terms in the $T(\varepsilon)$, we arrive at the expression

$$I_{\text{el}} = \frac{2e}{h} (\alpha_e - \alpha_o)^2 \int_{-\infty}^{\infty} d\varepsilon \varepsilon^2 \Delta f(\varepsilon). \quad (\text{C2})$$

To compute the integral Eq. (C2) we use the property of the Fourier transform. For the given function $\Delta f(\varepsilon)$, its Fourier transform is defined as

$$\Delta f(t) = \frac{1}{2\pi} \int_{-\infty}^{\infty} e^{-i\varepsilon t} \Delta f(\varepsilon) d\varepsilon. \quad (\text{C3})$$

Taking the n th derivative of Eq. (C3) at $t = 0$ we get

$$\int_{-\infty}^{\infty} \varepsilon^n \Delta f(\varepsilon) d\varepsilon = \frac{2\pi}{(-i)^n} \partial_t^n [\Delta f(t)]|_{t=0}. \quad (\text{C4})$$

Substituting Eq. (C4) for $n = 2$ into Eq. (C2), the elastic current is cast into the form

$$I_{\text{el}} = \frac{2e}{h} (\alpha_e - \alpha_o)^2 (-2\pi) \partial_t^2 [\Delta f(t)]|_{t=0}. \quad (\text{C5})$$

The Fourier transform of $\Delta f(\varepsilon)$ for $\mu_{L/R} = \pm eV/2$ is defined by

$$\Delta f(t) = T \frac{\sin\left(\frac{eVt}{2}\right)}{\sinh(\pi T t)}. \quad (\text{C6})$$

Substituting Eq. (C6) into Eq. (C5), we can easily arrive at the expression Eq. (22) for the elastic current at finite temperature

T , finite bias voltage V , and finite in-plane (Zeeman) magnetic field B [assuming $(T, eV, B) \ll T_K^o$],

$$\frac{I_{\text{el}}}{2e^2 V/h} = \left[B^2 + \frac{(eV)^2}{12} + \frac{(\pi T)^2}{3} \right] (\alpha_e - \alpha_o)^2. \quad (\text{C7})$$

APPENDIX D: NET ELECTRIC CURRENT

Here we present the details of the computation of the total electric current (the sum of the elastic and inelastic parts) given by Eq. (59). We discuss the total current in the linear-response (LR) and the beyond linear-response (BLR) regimes separately. The elastic part is given by Eq. (22) and the inelastic part which is composed of the four types of diagrams is expressed by Eq. (58).

1. LR

As discussed in the main text, both elastic and inelastic processes contribute to the LR current. The LR contribution of the elastic part is expressed by Eq. (22). The diagrams of type 1 and type 2 have the finite linear response contribution to the inelastic current. As detailed in Fig. 11, we have the expression of the total linear response current

$$\begin{aligned} \frac{\delta I^{\text{LR}}}{2e^2 V/h} \frac{1}{(\pi T)^2} &= \left[\frac{1}{3} (\alpha_e - \alpha_o)^2 \right]_{\text{LR elastic part}} + \left[\frac{A_T^{(1)}(\phi_e^2 + \phi_o^2) + 3A_T^{(1)}\Phi^2 + \frac{3A_T^{(2)}}{2}(\phi_e + \phi_o)\Phi - \frac{3A_T^{(2)}}{4}\Phi^2}{\text{LR inelastic part (type-1 and type-2 diagrams)}} \right] \\ &= \left[\frac{1}{3} (\alpha_e - \alpha_o)^2 + \frac{2}{3}(\phi_e^2 + \phi_o^2) - 2(\phi_e + \phi_o)\Phi + 3\Phi^2 \right] = \left[(\alpha_e - \alpha_o)^2 + 3\left(\Phi - \frac{2}{3}\alpha_e\right)\left(\Phi - \frac{2}{3}\alpha_o\right) \right]. \quad (\text{D1}) \end{aligned}$$

At the symmetry point the linear response contribution to the current given by Eq. (D1) exactly vanishes.

2. BLR

The BLR contribution of the elastic part is expressed by Eq. (22). The diagrams of type 3 and type 4 produce the finite contribution to the inelastic current only beyond the LR regime. In addition to the LR contribution, the type-1 and type-2 diagrams also contribute to nonlinear response. As detailed in Figs. 11 and 12, the total nonlinear current is

$$\begin{aligned} \frac{\delta I^{\text{BLR}}}{2e^2 V/h} \frac{1}{(eV)^2} &= \left[\frac{1}{12} (\alpha_e - \alpha_o)^2 \right]_{\text{BLR elastic part}} + \left[\frac{A_V^{(1)}(\phi_e^2 + \phi_o^2) + 3A_V^{(1)}\Phi^2 + \frac{3A_V^{(2)}}{2}(\phi_e + \phi_o)\Phi - \frac{3A_V^{(2)}}{4}\Phi^2}{\text{BLR inelastic part (type-1 and type-2 diagrams)}} \right] \\ &\quad + \left[\frac{A_V^{(4)}\phi_e\phi_o + 3A_V^{(3)}(\phi_e + \phi_o)\Phi + \frac{3}{2}(A_V^{(4)} - A_V^{(3)})\Phi^2}{\text{BLR inelastic part (type-3 and type-4 diagrams)}} \right] \\ &= \left[\frac{1}{12} (\alpha_e - \alpha_o)^2 + \frac{5}{12}(\phi_e^2 + \phi_o^2) - \frac{5}{4}(\phi_e + \phi_o)\Phi + \frac{15}{8}\Phi^2 + \frac{1}{2}\phi_e\phi_o - \frac{3}{4}(\phi_e + \phi_o)\Phi + \frac{9}{8}\Phi^2 \right] \\ &= \left[\frac{1}{2} (\alpha_e - \alpha_o)^2 + 3\left(\Phi - \frac{2}{3}\alpha_e\right)\left(\Phi - \frac{2}{3}\alpha_o\right) \right]. \quad (\text{D2}) \end{aligned}$$

The BLR contribution to the current expressed by Eq. (D2) goes to zero at the symmetry point $\alpha_e = \alpha_o = 3\Phi/2$.

The sum of the LR and BLR contributions results in Eq. (59). For completeness

$$\frac{\delta I}{2e^2 V/h} = 3[(\pi T)^2 + (eV)^2] \left(\Phi - \frac{2}{3}\alpha_e\right) \left(\Phi - \frac{2}{3}\alpha_o\right) + \left[(\pi T)^2 + \frac{1}{2}(eV)^2\right] (\alpha_e - \alpha_o)^2. \quad (\text{D3})$$

This equation represents in a simple and transparent form the contribution of the three FL constants to the charge transport.

$$\begin{aligned}
 \delta I_{\text{in}}^{\phi^2} &= \left[\text{type-1} \right] + \delta I_{\text{in}}^{\phi_o^2} \\
 &= \frac{2e^2V}{h} \left[A_V^{(1)}(eV)^2 + A_T^{(1)}(\pi T)^2 \right] (\phi_e^2 + \phi_o^2) \\
 \delta I_{\text{in}}^{\Phi^2} &= +\frac{1}{4} \left[\text{type-1} \right] \\
 &+ \frac{1}{4} \left[\text{type-1} \right] + 4 \left[\text{type-1} \right] + 4 \left[\text{type-1} \right] \\
 &+ \frac{1}{4} \left[\text{type-2} \right] - 2 \left[\text{type-2} \right] - 2 \left[\text{type-2} \right] \\
 &= \frac{6e^2V}{h} \left[\left(A_V^{(1)} - \frac{A_V^{(2)}}{4} \right) (eV)^2 + \left(A_T^{(1)} - \frac{A_T^{(2)}}{4} \right) (\pi T)^2 \right] \Phi^2 \\
 \delta I_{\text{in}}^{\phi_e \Phi} &= -\frac{1}{2} \left[\text{type-2} \right] + \delta I_{\text{in}}^{\phi_o \Phi} \\
 &= \frac{3e^2V}{h} \left[A_V^{(2)}(eV)^2 + A_T^{(2)}(\pi T)^2 \right] (\phi_e + \phi_o) \Phi
 \end{aligned}$$

FIG. 11. Feynman diagrams of type 1 and type 2 contributing to the charge current both in the linear response and beyond the linear response regimes. The coefficients computed in Secs. IV B 1 and IV B 2 take the following values: $A_T^{(1)} = 2/3$, $A_T^{(2)} = -4/3$, $A_V^{(1)} = 5/12$, and $A_V^{(2)} = -5/6$.

APPENDIX E: CALCULATION OF INTEGRALS

In this section we calculate two integrals that we used for the calculation of current correction contributed by the four types of diagram. The first integral to calculate is

$$\mathcal{I}_1 = \int_{-\infty}^{\infty} \frac{\cos^3\left(\frac{eV}{2}t\right) \sin\left(\frac{eV}{2}t\right)}{\sinh^4(\pi Tt)} dt. \quad (\text{E1})$$

The singularity of the integral in Eq. (E1) is removed by shifting the time contour by $i\gamma$ in the complex plane as shown in Fig. 13. The point splitting parameter γ is chosen to satisfy the conditions $\gamma D \gg 1$, $\gamma T \ll 1$, and $\gamma eV \ll 1$, where D is

$$\begin{aligned}
 \delta I_{\text{in}}^{\Phi^2} &= \frac{1}{4} \left[\text{type-4} \right] + \frac{1}{4} \left[\text{type-3} \right] - 2 \left[\text{type-3} \right] \\
 &+ \frac{1}{4} \left[\text{type-3} \right] - 2 \left[\text{type-3} \right] - 2 \left[\text{type-3} \right] \\
 &= \frac{3e^2V}{h} \left[\left(A_V^{(4)} - A_V^{(3)} \right) (eV)^2 + \left(A_T^{(4)} - A_T^{(3)} \right) (\pi T)^2 \right] \Phi^2 \\
 \delta I_{\text{in}}^{\phi_e \Phi} &= -\frac{1}{2} \left[\text{type-3} \right] \\
 &+ \delta I_{\text{in}}^{\phi_o \Phi} \\
 &= \frac{6e^2V}{h} \left[A_V^{(3)}(eV)^2 + A_T^{(3)}(\pi T)^2 \right] (\phi_e + \phi_o) \Phi \\
 \delta I_{\text{in}}^{\phi_e \phi_o} &= \left[\text{type-4} \right] = \frac{2e^2V}{h} \left[A_V^{(4)}(eV)^2 + A_T^{(4)}(\pi T)^2 \right] \phi_e \phi_o
 \end{aligned}$$

FIG. 12. Feynman diagrams of type 3 and type 4 contributing to the charge current beyond the linear response. The coefficients computed in Secs. IV B 3 and IV B 4 take the following values: $A_T^{(3)} = A_T^{(4)} = 0$, $A_V^{(3)} = -1/4$, and $A_V^{(4)} = 1/2$.

the band cutoff. Then Eq. (E1) can be written as

$$\begin{aligned}
 \mathcal{I}_1^+ &= \int_{-\infty+i\gamma}^{\infty+i\gamma} \frac{\cos^3(at) \sin(at)}{\sinh^4(\pi Tt)} dt \\
 &= -\frac{i}{16} [\mathcal{Z}(4a, T) - \mathcal{Z}(-4a, T) + 2\mathcal{Z}(2a, T) \\
 &\quad - 2\mathcal{Z}(-2a, T)]. \quad (\text{E2})
 \end{aligned}$$

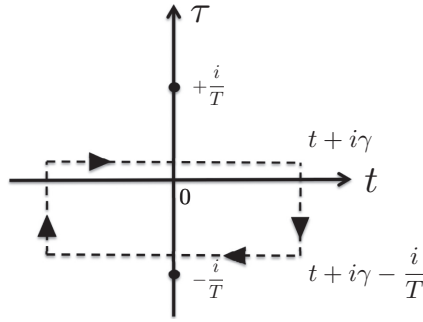


FIG. 13. The contour of the integration for the integral Eq. (E1) with negative shift.

In Eq. (E2), $a = eV/2$ and we introduced the shorthand notation

$$\mathcal{Z}(a, T) = \int_{-\infty+i\gamma}^{\infty+i\gamma} \frac{e^{iat}}{\sinh^4(\pi T t)} dt = \int_{-\infty+i\gamma}^{\infty+i\gamma} h(a, T; t) dt. \quad (\text{E3})$$

The poles of the integrand $h(a, T; t)$ in Eq. (E3) are

$$\pi T t = \pm im\pi \Rightarrow t = \pm \frac{im}{T}, \quad m = 0, \pm 1, \pm 2, \pm 3 \dots \quad (\text{E4})$$

The integration of $h(a, T; t)$ over the rectangular contour Fig. 13 shifted by i/T upon using the Cauchy residue theorem results in

$$\mathcal{Z}(a, T) = \int_{-\infty+i\gamma}^{\infty+i\gamma} \frac{e^{ia(t-i/T)}}{\sinh^4[\pi T(t - \frac{i}{T})]} dt - 2\pi i \text{Res}[h(a, T; t)]|_{t=0}, \quad (\text{E5})$$

where “Res” stands for the residue. By expanding the sinh function in Eq. (E5) we get

$$\mathcal{Z}(a, T)(1 - e^{a/T}) = -2\pi i \text{Res}[h(a, T; t)]|_{t=0}. \quad (\text{E6})$$

By using the standard formula for the calculation of the residue, Eq. (E6) casts the form

$$\mathcal{Z}(a, T) = -\frac{2\pi(a^3 + 4a(\pi T)^2)}{6(\pi T)^4} \frac{1}{1 - e^{a/T}}. \quad (\text{E7})$$

Substituting Eq. (E7) into Eq. (E2) gives the required integral

$$\mathcal{I}_1^+ = \frac{i\pi}{(\pi T)^4} \frac{eV}{2} \left[\frac{5}{12}(eV)^2 + \frac{2}{3}(\pi T)^2 \right]. \quad (\text{E8})$$

Choosing the contour with the negative shift results in the integral \mathcal{I}_1^- such that $\mathcal{I}_1^- = -\mathcal{I}_1^+$. As a result

$$\mathcal{I}_1^\pm(V, T) = \pm \frac{i\pi}{(\pi T)^4} \frac{eV}{2} \left[\frac{5}{12}(eV)^2 + \frac{2}{3}(\pi T)^2 \right]. \quad (\text{E9})$$

The second integral that we are going to compute is

$$\mathcal{I}_2 = \int_{-\infty}^{\infty} \frac{\cos(\frac{eV}{2}t) \sin^3(\frac{eV}{2}t)}{\sinh^4(\pi T t)} dt. \quad (\text{E10})$$

In the same way and using the same notations as for the first integral, Eq. (E10) reads

$$\begin{aligned} \mathcal{I}_2^+ &= \frac{i}{16} [\mathcal{Z}(4a, T) - \mathcal{Z}(-4a, T) - 2\mathcal{Z}(2a, T) + 2\mathcal{Z}(-2a, T)] \\ &= -\frac{i\pi}{(\pi T)^4} \left(\frac{eV}{2} \right)^3. \end{aligned} \quad (\text{E11})$$

Similar to Eq. (E9), the integral \mathcal{I}_2 takes the form

$$\mathcal{I}_2^\pm(V, T) = \mp \frac{i\pi}{(\pi T)^4} \left(\frac{eV}{2} \right)^3. \quad (\text{E12})$$

For the calculations of all diagrams we used the corresponding results of contour integration with positive shift.

-
- [1] P. Nozieres and A. Blandin, *J. Phys.* **41**, 193 (1980).
[2] J. Kondo, *Prog. Theor. Phys.* **32**, 37 (1964).
[3] A. A. Abrikosov, *Physics* **2**, 5 (1965).
[4] H. Shul, *Physics* **2**, 39 (1965).
[5] P. W. Anderson and G. Yuval, *Phys. Rev. Lett.* **23**, 89 (1969).
[6] P. W. Anderson, G. Yuval, and D. R. Hamann, *Phys. Rev. B* **1**, 4464 (1970).
[7] A. A. Abrikosov and A. A. Migdal, *J. Low Temp. Phys.* **3**, 519 (1970).
[8] M. Fowler and A. Zawadowski, *Solid State Commun.* **9**, 471 (1971).
[9] P. Nozières, *J. Low Temp. Phys.* **17**, 31 (1974).
[10] I. Affleck, *Nucl. Phys. B* **336**, 517 (1990).
[11] A. M. Tsvelik and P. B. Wiegmann, *Adv. Phys.* **32**, 453 (1983).
[12] N. Andrei, K. Furuya, and J. H. Lowenstein, *Rev. Mod. Phys.* **55**, 331 (1983).
[13] P. D. Sacramento and P. Schlottmann, *J. Phys.: Condens. Matter* **3**, 9687 (1991).
[14] D. L. Cox and A. Zawadowski, *Adv. Phys.* **47**, 599 (1998).
[15] S. Sasaki, S. De Franceschi, J. M. Elzerman, W. G. van der Wiel, M. Eto, S. Tarucha, and L. P. Kouwenhoven, *Nature (London)* **405**, 764 (2000).
[16] M. Eto and Y. V. Nazarov, *Phys. Rev. Lett.* **85**, 1306 (2000).
[17] M. Pustilnik and L. I. Glazman, *Phys. Rev. Lett.* **87**, 216601 (2001).
[18] M. Pustilnik, L. I. Glazman, D. H. Cobden, and L. P. Kouwenhoven, *Lect. Notes Phys.* **579**, 3 (2001).
[19] A. Kogan, G. Granger, M. A. Kastner, D. Goldhaber-Gordon, and H. Shtrikman, *Phys. Rev. B* **67**, 113309 (2003).
[20] M. Pustilnik and L. Glazman, *J. Phys.: Condens. Matter* **16**, R513 (2004).
[21] C. H. L. Quay, J. Cumings, S. J. Gamble, R. de Picciotto, H. Kataura, and D. Goldhaber-Gordon, *Phys. Rev. B* **76**, 245311 (2007).
[22] S. Di Napoli, M. A. Barral, P. Roura-Bas, L. O. Manuel, A. M. Llois, and A. A. Aligia, *Phys. Rev. B* **92**, 085120 (2015).

- [23] A. Hewson, *The Kondo Problem to Heavy Fermions* (Cambridge University Press, Cambridge, England, 1993).
- [24] I. Affleck and A. W. W. Ludwig, *Phys. Rev. B* **48**, 7297 (1993).
- [25] P. Coleman, L. B. Ioffe, and A. M. Tsvelik, *Phys. Rev. B* **52**, 6611 (1995).
- [26] N. Andrei and C. Destri, *Phys. Rev. Lett.* **52**, 364 (1984).
- [27] A. Posazhennikova and P. Coleman, *Phys. Rev. Lett.* **94**, 036802 (2005).
- [28] W. Koller, A. C. Hewson, and D. Meyer, *Phys. Rev. B* **72**, 045117 (2005).
- [29] L. Kouwenhoven and L. Glazman, *Phys. World* **14**, 33 (2001).
- [30] M. Pustilnik and L. I. Glazman, *Phys. Rev. B* **64**, 045328 (2001).
- [31] W. Hofstetter and H. Schoeller, *Phys. Rev. Lett.* **88**, 016803 (2001).
- [32] M. Pustilnik, L. I. Glazman, and W. Hofstetter, *Phys. Rev. B* **68**, 161303(R) (2003).
- [33] W. Hofstetter and G. Zarand, *Phys. Rev. B* **69**, 235301 (2004).
- [34] Z. Iftikhar, S. Jezouin, A. Anthore, U. Gennser, F. D. Parmentier, A. Cavanna, and F. Pierre, *Nature (London)* **526**, 233 (2015).
- [35] A. J. Keller, L. Peeters, C. P. Moca, I. Weymann, D. Mahalu, V. Umansky, G. Zaránd, and D. Goldhaber-Gordon, *Nature (London)* **526**, 237 (2015).
- [36] R. M. Potok, I. G. Rau, H. Shtrikman, Y. Oreg, and D. Goldhaber-Gordon, *Nature (London)* **446**, 167 (2007).
- [37] D. C. Ralph and R. A. Buhrman, *Phys. Rev. Lett.* **69**, 2118 (1992).
- [38] D. C. Ralph and R. A. Buhrman, *Phys. Rev. B* **51**, 3554 (1995).
- [39] W. G. van der Wiel, S. DeFranceschi, J. M. Elzerman, S. Tarucha, L. P. Kouwenhoven, J. Motohisa, F. Nakajima, and T. Fukui, *Phys. Rev. Lett.* **88**, 126803 (2002).
- [40] K. A. Matveev, *Phys. Rev. B* **51**, 1743 (1995).
- [41] A. Rosch, J. Kroha, and P. Wolfle, *Phys. Rev. Lett.* **87**, 156802 (2001).
- [42] Y. Oreg and D. Goldhaber-Gordon, *Phys. Rev. Lett.* **90**, 136602 (2003).
- [43] A. Posazhennikova, B. Bayani, and P. Coleman, *Phys. Rev. B* **75**, 245329 (2007).
- [44] Y. Kleeorin and Y. Meir, [arXiv:1710.05120](https://arxiv.org/abs/1710.05120).
- [45] J. R. Schrieffer and P. Wolf, *Phys. Rev.* **149**, 491 (1966).
- [46] L. I. Glazman and M. E. Raikh, *Pis'ma Zh. Eksp. Teor. Fiz.* **47**, 378 (1988) [*JETP Lett.* **47**, 452 (1988)].
- [47] For the sake of simplicity we assume certain symmetry in the dot-leads junction. Namely, the new basis diagonalizing the Hamiltonian Eq. (2) corresponds to symmetric (even) and antisymmetric (odd) combinations of the states in the L - R leads. The effects of coupling asymmetry can straightforwardly be accounted by using methods developed in Ref. [57].
- [48] S. Tarucha, D. G. Austing, Y. Tokura, W. G. van der Wiel, and L. P. Kouwenhoven, *Phys. Rev. Lett.* **84**, 2485 (2000).
- [49] P. W. Anderson, *J. Phys. C* **3**, 2436 (1970).
- [50] M. Hanl, A. Weichselbaum, J. von Delft, and M. Kiselev, *Phys. Rev. B* **89**, 195131 (2014).
- [51] C. Mora, *Phys. Rev. B* **80**, 125304 (2009).
- [52] C. Mora, C. P. Moca, J. von Delft, and G. Zaránd, *Phys. Rev. B* **92**, 075120 (2015).
- [53] M. Filippone, C. P. Moca, J. von Delft, and C. Mora, *Phys. Rev. B* **95**, 165404 (2017).
- [54] A. O. Gogolin, A. A. Nersesyan, and A. M. Tsvelik, *Bosonization and Strongly Correlated Systems* (Cambridge University Press, Cambridge, 1998).
- [55] I. Affleck, *Acta Phys. Polon. B* **26**, 1869 (1995).
- [56] C. Mora, X. Leyronas, and N. Regnault, *Phys. Rev. Lett.* **100**, 036604 (2008).
- [57] C. Mora, P. Vitushinsky, X. Leyronas, A. A. Clerk, and K. Le Hur, *Phys. Rev. B* **80**, 155322 (2009).
- [58] P. Vitushinsky, A. A. Clerk, and K. Le Hur, *Phys. Rev. Lett.* **100**, 036603 (2008).
- [59] C. B. M. Hørig, C. Mora, and D. Schuricht, *Phys. Rev. B* **89**, 165411 (2014).
- [60] Y. M. Blanter and Y. V. Nazarov, *Quantum Transport: Introduction to Nanoscience* (Cambridge University Press, Cambridge, England, 2009).
- [61] D. B. Karki and M. N. Kiselev, *Phys. Rev. B* **96**, 121403(R) (2017).
- [62] L. V. Keldysh, *Sov. Phys. JETP* **20**, 1018 (1965).
- [63] D. B. Karki and M. N. Kiselev (unpublished).
- [64] F. Bauer, J. Heyder, E. Schubert, D. Borowsky, D. Taubert, B. Bruognolo, D. Schuh, W. Wegscheider, J. von Delft, and S. Ludwig, *Nature (London)* **501**, 73 (2013).
- [65] J. Heyder, F. Bauer, E. Schubert, D. Borowsky, D. Schuh, W. Wegscheider, J. von Delft, and S. Ludwig, *Phys. Rev. B* **92**, 195401 (2015).
- [66] T. Rejec and Y. Meir, *Nature (London)* **442**, 900 (2006).
- [67] P. Coleman, *Introduction to Many-Body Physics* (Cambridge University Press, Cambridge, 2015).
- [68] L. S. Levitov and G. B. Lesovik, *JETP Lett.* **58**, 230 (1993).
- [69] L. S. Levitov, *Quantum Noise in Mesoscopic Systems*, edited by Y. V. Nazarov (Kluwer, Dordrecht, 2003).
- [70] A. Oguri and A. C. Hewson, *Phys. Rev. Lett.* **120**, 126802 (2018).
- [71] A. Oguri and A. C. Hewson, *Phys. Rev. B* **97**, 045406 (2018).
- [72] A. Oguri and A. C. Hewson, *Phys. Rev. B* **97**, 035435 (2018).